HHS Public Access

Author manuscript

Sci Transl Med. Author manuscript; available in PMC 2017 August 23.

Published in final edited form as:

Sci Transl Med. 2016 November 30; 8(367): 367ra167. doi:10.1126/scitranslmed.aaf2335.

Internalization of secreted antigen–targeted antibodies by the neonatal Fc receptor for precision imaging of the androgen receptor axis

Daniel L. J. Thorek[1,2], **Philip A. Watson**[3,*], **Sang-Gyu Lee**[2,*], **Anson T. Ku**[2], **Stylianos Bournazos**[4], **Katharina Braun**[5], **Kwanghee Kim**[6], **Kjell Sjöström**[7], **Michael G. Doran**[2], **Urpo Lamminmäki**[8], **Elmer Santos**[2], **Darren Veach**[2,9], **Mesruh Turkekul**[10], **Emily Casey**[11], **Jason S. Lewis**[11,12], **Diane S. Abou**[1], **Marise R. H. van Voss**[1,13], **Peter T. Scardino**[6,14], **Sven-Erik Strand**[15], **Mary L. Alpaugh**[16], **Howard I. Scher**[17,18], **Hans Lilja**[6,17,19,20,21,†], **Steven M. Larson**[2,9,†], and **David Ulmert**[6,11,22,†]

[1]Division of Nuclear Medicine and Molecular Imaging, Department of Radiology and Radiological Science, Sidney Kimmel Comprehensive Cancer Center, Johns Hopkins School of Medicine, Baltimore, MD 21205, USA [2]Nuclear Medicine Service, Department of Radiology, Memorial Sloan Kettering Cancer Center, New York, NY 10065, USA [3]Human Oncology and Pathogenesis Program, Memorial Sloan Kettering Cancer Center, New York, NY 10065, USA [4]Leonard Wagner Laboratory of Molecular Genetics and Immunology, Rockefeller University, New York, NY 10065, USA [5]Department of Urology, University Hospital of the Ruhr-University of Bochum, Marien Hospital Herne, Herne, Germany [6]Urology Service, Department of Surgery, Memorial Sloan Kettering Cancer Center, New York, NY 10065, USA [7]Innovagen AB, Lund, Sweden [8]Department of Biochemistry, University of Turku, Turku, Finland [9]Department of Radiology, Weill Cornell Medical College, New York, NY10065, USA [10]Molecular Cytology Core Facility, Sloan Kettering Institute, Memorial Sloan Kettering Cancer Center, New York, NY 10065, USA [11]Molecular Pharmacology and Chemistry Program, Memorial Sloan Kettering Cancer Center, New York, NY 10065, USA [12]Radiochemistry and Imaging Sciences Service, Department of Radiology, Memorial Sloan Kettering Cancer Center, New York, NY 10065, USA [13]Department of Pathology,

[†]Corresponding author. ulmerth@mskcc.org (D.U.); liljah@mskcc.org (H.L.); larsons@mskcc.org (S.M.L.).
[*]These authors contributed equally to this work.

SUPPLEMENTARY MATERIALS

www.sciencetranslationalmedicine.org/cgi/content/full/8/367/367ra167/DC1
Materials and Methods
Reference (51)

Author contributions: D.L.J.T. and D.U. conceived the study, designed and executed the characterization, imaging, and monitoring using 11B6, analyzed the data, and wrote the paper. P.A.W. performed analysis of RT-PCR and advised on the use of advanced models. S.-G.L. performed confocal microscopy experiments. A.T.K., K.B., K.K., M.G.D., M.T., E.C., K.S., U.L., and M.R.H.v.V. assisted in cellular and animal models and experimentation, and D.V. and D.S.A. assisted in probe synthesis. S.B., E.S., J.S.L., P.T.S., S.-E.S., M.L.A., H.I.S., H.L., and S.M.L. assisted in experimental design and helped write the manuscript.

Competing interests: D.L.J.T., D.U., S.-E.S., and H.L. are shareholders of Diaprost Inc. D.LJ.T., S.-E.S., and D.U. currently serve as board members of Diaprost Inc. D.L.J.T., A.K., S.-E.S., S.M.L., and D.U. are inventors on a patent (62257179)submitted by the MSKCC that covers systems, methods, and compositions for imaging AR axis activity in carcinoma. D.U. is also the inventor on a patent(20060182682) held by Diaprost Inc. that covers diagnostic imaging of PCa using 11B6. S.-E.S. and U.L. are inventors on a patent application (WO2015075445) submitted by Diaprost Inc. that covers the humanized anti-hK2 antibody.

Data and materials availability: The humanized antibodies hu11B6 and hu5A10 are available from S.-E.S. under a material agreement with the Lund University.

University Medical Center Utrecht, Utrecht, Netherlands [14]Department of Urology, Weill Cornell Medical College, New York, NY 10065, USA [15]Department of Medical Radiation Physics, Lund University, Lund, Sweden [16]Departments of Biology and Biomedical and Translational Sciences, Rowan University, Glassboro, NJ 08028, USA [17]Genitourinary Oncology Service, Department of Medicine, Memorial Sloan Kettering Cancer Center, New York, NY 10065, USA [18]Department of Medicine, Weill Cornell Medical College, New York, NY 10065, USA [19]Department of Laboratory Medicine, Memorial Sloan Kettering Cancer Center, New York, NY 10065, USA [20]Nuffield Department of Surgical Sciences, University of Oxford, Oxford, UK [21]Department of Laboratory Medicine, Lund University, Malmö, Sweden [22]Division of Urological Research, Department of Clinical Sciences, Lund University, Malmö, Sweden

Abstract

Targeting the androgen receptor (AR) pathway prolongs survival in patients with prostate cancer, but resistance rapidly develops. Understanding this resistance is confounded by a lack of noninvasive means to assess AR activity in vivo. We report intracellular accumulation of a secreted antigen-targeted antibody (SATA) that can be used to characterize disease, guide therapy, and monitor response. AR-regulated human kallikrein-related peptidase 2 (free hK2) is a prostate tissue-specific antigen produced in prostate cancer and androgen-stimulated breast cancer cells. Fluorescent and radio conjugates of 11B6, an antibody targeting free hK2, are internalized and noninvasively report AR pathway activity in metastatic and genetically engineered models of cancer development and treatment. Uptake is mediated by a mechanism involving the neonatal Fc receptor. Humanized 11B6, which has undergone toxicological tests in nonhuman primates, has the potential to improve patient management in these cancers. Furthermore, cell-specific SATA uptake may have a broader use for molecularly guided diagnosis and therapy in other cancers.

INTRODUCTION

Activation of the androgen receptor (AR) signaling axis contributes to prostate cancer (PCa) progression throughout the entire course of the disease, including the terminal castration-resistant state (1). After initial response to inhibition with androgen deprivation treatment, which is a mainstay of PCa treatment, AR pathway reactivation inevitably occurs. This has been attributed to gene amplification (2), intratumoral androgen synthesis (3), constitutively active variants, and other mechanisms (2, 4). AR is also differentially expressed in several breast cancer (BCa) subtypes, although without a clearly defined role (5, 6). One subtype is aggressive triple-negative BCa (TNBC) in which emerging studies suggest that AR expression may be correlated with decreased survival (7). Recent trials have focused on AR inhibition as an approach to stabilize TNBC (8, 9) for which there are no targeted treatment options. Thus, quantifying lesion-specific AR pathway activity represents a critical unmet need: that it would assist in treatment selection and serve as a pharmacodynamic marker of pathway inhibition and as a non-invasive marker of therapeutic efficacy. Although the prostate-specific antigen (PSA), which is a commonly used biomarker of PCa, is AR-dependent, PSA concentrations in the blood are also affected by the degree of tumor

differentiation, physiological factors, and total tumor burden, making PSA unsuitable as a measure of pathway activation.

The approach of treating disease with drugs that bind to secreted antigens (for example, antibodies directed to growth factors) is a firmly established strategy in clinical practice. Targets of such biologics include vascular endothelial growth factor (10,11), receptor activator of nuclear factor κB (12), and tissue necrosis factor (13). However, imaging agents or drug conjugates directed to secreted antigens have been far less successful because antibody-bound complexes wash out of the disease site (14,15). This has limited targets for PCa to cell-surface receptors, which usually have poor tissue- or disease-restricted expression (fig. S1, A to C), as indicated from the integrated in silico transcriptomics database (MediSapiens).

Here, we report an approach using an antibody (11B6) directed to an epitope accessible only on the free, catalytically active form of human kallikrein-related peptidase 2 (hK2). When 11B6 is bound to active hK2, this complex is permanently internalized and transported to lysosomal compartments. hK2 is a trypsin-like enzyme with AR-driven expression specific to prostate, PCa, and AR-positive BCa tissues. hK2 is activated by TMPRSS2 and secreted into the ducts of the prostate where it initiates a cascade to cleave semenogelin, which is the extracellular matrix in the ejaculate, to enhance sperm motility (16). hK2 in man is exclusively expressed in prostatic tissues (fig. S1D). As with PSA, retrograde release of catalytically inactive hK2 into the blood occurs when the highly structured organization of the prostate is compromised upon hypertrophy or malignant transformation. Despite the homology similarity between the kallikreins, 11B6 is specific for hK2 and does not bind PSA (17).

The observed 11B6 uptake in free hK2-producing cancer cells is a process facilitated by the neonatal Fc receptor (FcRn). This feature is recapitulated in AR-positive BCa models treated by hormones that stimulate hK2 production, demonstrating that 11B6 has the ability to profile and monitor AR activity in two commonly diagnosed cancers, PCa and some types of BCa. In these analyses, we have applied 11B6 for both positron emission tomography (PET) and fluorescence imaging in xenograft and genetically engineered mouse models (GEMM) for disease detection to (i) quantitatively assess AR pathway activity, (ii) determine pharmacodynamic parameters, (iii) evaluate treatment efficacy in immunocompetent models, and (iv) guide treatment in clinically relevant scenarios.

Already adapted for near-term clinical translation, 11B6 immunoimaging resolves issues at key clinical decision points for both PCa and BCa patients to improve management. We also show that the FcRn-mediated uptake mechanism can be used to facilitate uptake by other secreted antigen-targeted antibodies (SATA).

RESULTS

Correlation of anti-hK2 imaging with hK2 expression

hK2 is an anatomically restricted and disease-restricted protein (16). We attempted to apply a murine antibody with specificity for the catalytic pocket of free hK2 for immunotargeted

PET (immunoPET) to visualize expression noninvasively. Conjugation to desferrioxamine B (DFO) and subsequent zirconium-89 labeling yielded ^{89}Zr-11B6, a PET radiotracer. A competition binding assay was conducted, revealing that bioconjugation of 11B6 resulted in no significant loss of affinity for hK2 (fig. S2 and tables S1 to S3). In vitro studies of ^{89}Zr-11B6 uptake showed expression-specific uptake, and specificity was verified by blocking with excess 11B6. Activity after washing revealed that this SATA was internalized by hK2-expressing cells.

To test whether the uptake occurred in vivo, we first optimized the dose of ^{89}Zr-11B6 with an escalation study and PET quantification in mice bearing human PCa xenografts (Fig. 1, A to C). The time to tumor saturation inversely correlated with tracer mass and improved tumor/blood contrast: 2.4, 4.2, 7.7, and 13.7 hours for 300, 150, 50, and 15 μg of ^{89}Zr-11B6, respectively. Subsequent experiments used 50 μg of^{89}Zr-11B6, which achieved a plateau in tumor uptake (saturation) with low background activity after 120 hours (Fig. 1C). Uptake was correlated to hK2 protein expression (fig. S3A), and in vivo specificity was verified by blocking with 1 mg of unlabeled 11B6 and using hK2-negative DU145 xenografts (table S4). To assess the potential for imaging of patients who have failed hormone therapy, we also measured the uptake in castration-resistant 22Rv1 tumor xenografts. Here, we also observed robust localization to the tumor through continued AR-driven hK2 expression (fig. S3B).

KLK2 expression was evaluated in seven xenograft lines (fig. S4A). VCaP exhibited the highest *KLK2* expression and showed markedly higher ^{89}Zr-11B6 internalization [80.7 percent injected activity per gram (%IA/g)] compared to LNCaP (24.7 %IA/g) (Fig. 1D), demonstrating the ability to determine hK2 expression status in vivo. The expression of *KLK2* did not correlate with two other AR-governed imaging targets, *KLK3* (PSA) or *FOLH1* (prostate-specific membrane antigen), confirming that hK2 is a distinct biomarker (fig. S4).

Although the PSA concentration in blood is AR-dependent, the value is a function of degree of tumor differentiation, location, and total tumor burden, making it unsuitable as a measure of pathway activation. Direct imaging of AR abundance and measurement of receptor occupancy have previously been achieved using ^{18}F-FDHT (16β-[^{18}F] fluoro-5α-dihydrotestosterone) [a radiolabeled analog of the androgen dihydrotestosterone (DHT) (18, 19)]. However, the uptake of this agent does not correlate with PSA decline or response, both of which are fundamentally tied to AR pathway activity and not simply to the amount of receptor. In the VCaP PCa model, the rapid metabolism (20) and abdominal clearance of the agent (fig. S5) result in limited contrast of the tumor to the background structures.

Delineating bone metastases

Both PCa and BCa commonly metastasize to the skeleton, often manifesting a mixed bone-forming/resorbing phenotype that complicates detection because current clinical imaging methods rely on the uptake at sites with increased osteoblastic activity (21, 22). We evaluated the ability of ^{89}Zr-11B6 to detect both phenotypes using intraosseous LNCaP-AR (osteolytic) and VCaP (osteoblastic) bone metastases models with control PC3 (AR/hK2-negative osteolytic) bone lesions (Fig. 2). ^{89}Zr-11B6 PET demonstrated robust delineation in

both osteometastatic phenotypes of AR-positive disease, with the uptake delayed relative to subcutaneously inoculated tumors (fig. S6).

Faithful recapitulation of PCa for study in mice is particularly difficult given the absence of murine orthologs of several human prostate-specific genes, including prostate kallikreins (16). To test tracer kinetics in an immunocompetent milieu and measure the uptake in autochthonous mouse tumors, we cloned a prostate full-length *KLK2* construct encoding pre-pro-hK2 under the control of the probasin promoter (Pb_*KLK2*), enabling prostate-specific and androgen-driven expression of hK2. Using B6 mice as negative controls, ^{89}Zr-11B6 uptake was specific to hK2-positive prostatic tissue in vivo (fig. S7).

Internalization of 11B6 by FcRn

To investigate SATA internalization, we first evaluated conjugated 11B6 in whole-mount sections of prostate tissue from Pb_*KLK2* mice. A high concordance between intravenously administered fluorescent and radioactive tracer was observed, as was an association between antibody uptake and staining for AR (Fig. 3, A to E). 11B6 in the lumen of prostatic ducts suggested uptake by epithelial cells, as confirmed by confocal microscopy (Fig. 3B and video S1). To verify, we analyzed single cells extracted from this tissue for fluorescent antibody uptake. In addition, we performed analysis of PCa cell lines in vitro (fig. S8).

FcRn generally facilitates antigen recognition in luminal structures throughout the body (23) and is expressed in a large set of PCa lines (fig. S9). Intracellular transport of the conjugate was determined by costaining PCa cells for FcRn and anti-immunoglobulin G (IgG). After pulsed exposure, 11B6 was associated with FcRn during the early phase of uptake. At later time points, 11B6 appeared intracellularly, and FcRn had returned to the cell membrane. The 11B6-hK2 complex was shuttled from physiological pH early endosomes to acidic late endosomes, as shown using a pH-responsive dye conjugated to 11B6 and imaged in live cells (Fig. 3, F and G).

To confirm the specific role of FcRn in the internalization of the SATA-antigen complex, we generated recombinant mutant 11B6 IgG_1 (modified at His^{435} to Ala; H435A-11B6) to abrogate FcRn binding (24) and compared the cellular uptake in physiological and acidified medium (25). This mutation abrogates FcRn binding but does not affect variable region recognition or affinity. As expected, surface plasmon resonance (SPR) affinity of FcRn for 11B6 was pH-dependent and absent in the H435A-11B6 mutant (fig. S10A). In culture, incubation at acidic pH conditions, as found in tumors and the prostate (26), augmented internalization (fig. S10B). The presence of both FcRn and hK2 was required for internalization, and isotype-matched control antibody did not bind cells or transport intracellularly through endosomes (fig. S11).

^{89}Zr-labeled 11B6 and mutant Fc antibody were applied to establish FcRn dependence in vivo. Uptake of the mutant Fc antibody matched that of control nonspecific IgG (shown for LNCaP; fig. S12, A and B), despite retained immunoreactivity of the FcRn binding-deficient antibody (fig. S12C). Relative to the wild-type 11B6 antibody, H435A-11B6 uptake in immunodeficient xenograft models was significantly lower [21.2 % IA/g for VCaP ($P = 5.97 \times 10^{-5}$) and 5.23 %IA/g for LNCaP ($P = 8.24 \times 10^{-7}$); fig. S12D]. Antibody function and

pharmacokinetics are dependent on host interactions. Therefore, we also assessed the uptake in immunocompetent GEMM of adenocarcinoma [obtained by crossing Pb_*KLK2* with ARR2/probasin-*Myc* (Hi-*Myc*)(27)]. As expected, we observed an accumulation of 11B6 in the transformed lobe of the prostate. In contrast, the uptake of FcRn binding-deficient H435A-11B6 was abolished (fig. S12, E and F).

FcRn is widely expressed in tissues throughout the body and particularly concentrated in the liver (28). Antibody imaging in this organ is difficult because nonspecific uptake and clearance increase the background. To rigorously evaluate the ^{89}Zr-11B6 agent, we sought to test whether metastasis of PCa to the liver could be identified because this is an end-stage site of disseminated PCa. ^{89}Zr-11B6 PET and magnetic resonance imaging (MRI) revealed specific focal accumulation in hK2-expressing LREX′ metastases in the liver that were resistant to enzalutamide, a second-generation AR antagonist (fig. S13). Autoradiography and histopathological findings correlated with the noninvasive assessment.

We also tested whether the uptake of antibody-secreted antigen complexes could be applied to other targets. Previously, we have shown that targeting free PSA with an antibody (5A10) can delineate subcutaneous xenografts. The uptake was transient because the SATA-antigen complex was not internalized and washed out of the tumor microenvironment (15). Previously identified residues at the constant heavy chain 2 and 3 (CH2/CH3) junction contribute to the pH-dependent affinity of the IgG interaction with FcRn, suggesting multiple possible explanations for the inability of 5A10 to bind FcRn. We grafted the complementarity-determining regions (CDRs) of 5A10 onto the 11B6 Fc scaffold (bearing the His^{435};5A10$^{H435\text{-}wt}$) (29). In vivo, we observed steadily increasing tumor uptake using ^{89}Zr-5A10$^{H435\text{-}wt}$ in LNCaP xenografts in contrast to the original PSA-targeting 5A10 (fig. S14).

Anti-hK2 uptake in BCa

KLK2 expression is restricted to the prostate and PCa tissues in man; however, hK2 and PSA are also detectable in (female) BCa cell lines (30) and primary patient samples, including serum and nipple aspirate fluid, after appropriate activation of the AR pathway by steroid hormones (31, 32). We investigated whether FcRn-mediated internalization of the antibody-bound hK2 is prostate-specific. In the presence of DHT, a subset of AR-positive BCa lines secretes hK2, including the TNBC line MFM-223 (fig. S15, A and B, and table S5). Androgen stimulation increased the AR-responsive *KLK2* (fig. S15, C and D).

To assess whether 11B6 could be internalized in a non-prostate-derived cancer model, we used ^{89}Zr-11B6 to image AR-positive BCa with BT474 (ER$^+$/PR$^+$/HER2$^+$/AR$^+$) xenografts. ^{89}Zr-11B6 uptake was significantly greater in DHT-treated female mice compared to estrogen alone ($P = 0.001$; fig. S15E). As above, confocal microscopy revealed that BT474 cells with and without DHT treatment internalize 11B6 in a time-dependent manner (fig. S16).

Staging adenocarcinoma and monitoring treatment

We next applied ^{89}Zr-11B6 PET to detect and monitor tumor progression in the prostate of transgenic models of adenocarcinoma (Fig. 4). Greater SATA uptake at sites of disease was

noted, demonstrating heterogeneous progression even at the small scale of the mouse prostate. Quantitation of tracer accumulation in the prostate corresponded with transformation from prostatic intraepithelial neoplasia to adenocarcinoma. Ex vivo autoradiography of tracer microdistribution and histological adenocarcinoma is shown for a 50-week-old mouse (fig. S17).

Use of the anti-hK2 tracer to assess AR activity in response to intervention was studied in three clinical scenarios that currently lack (but would greatly benefit from) a molecularly specific assessment. In the first substudy, ^{89}Zr-11B6 was measured before and after surgical castration in a bone metastasis model using LNCaP-AR/luc (expressing luciferase under the control of ARR2-Pb). Standard-of-care blood measurements of PSA and ^{18}F-sodium fluoride (^{18}F-NaF) PET bone scans were compared to hK2-targeted PET imaging. ^{89}Zr-11B6 uptake decreased after castration ($P = 0.005$; Fig. 5, A and B, and table S6), as did AR-driven luciferase ($P = 0.0012$; Fig. 5C). Conventional metrics of PCa bone lesion response, including PSA (Fig. 5D) and ^{18}F-NaF (Fig. 5, E and F, and table S6), remained unchanged.

The second scenario simulated intermittent androgen deprivation therapy. There is considerable debate concerning the optimal treatment regimen (intermittent or continuous inhibition) for hormonal therapy (33). Pb_*KLK2* × Hi-*Myc* mice received depot injections of degarelix, a gonadotropin-releasing hormone (GnRH) antagonist, ablating androgen production for 2 months. ^{89}Zr-11B6 imaging was performed longitudinally to assess the response to androgen deprivation and reactivation after discontinuation. ^{89}Zr-11B6 decreased after castration but reemerged at the end of the treatment period, enabling readout of pharmacodynamic inhibition of the AR pathway (fig. S18).

Our final clinical simulation involved noninvasive imaging of the impact of different degrees of inhibition on AR activity in the tumor (intratumoral) and prostate itself (intraprostatic). We initially monitored progression of disease in 14 Pb_*KLK2* ×Hi-*Myc* mice using ^{89}Zr-11B6 PET. Thereafter, mice were randomized into three treatment groups: vehicle ($n = 4$), castration ($n = 6$), or castration plus enzalutamide ($n = 4$). We noted substantial heterogeneity in the individual animals' prostatic uptake of the tracer during progression and in response to therapy (Fig.6, A to C).

SATA uptake was repressed during the last months of treatment in mice receiving adjuvant AR blockade, indicating a benefit for adjuvant AR blockade using antiandrogens in the postcastration setting (Fig. 6, D and E). As suspected, reverse transcription polymerase chain reaction (RT-PCR) analysis of prostatic tissue harvested from treated mice displayed significantly lower *KLK2* expression ($P = 0.0016$ for castrate alone and $P = 0.0089$ for castration and enzalutamide; fig. S19A). Expression differences with and without adjuvant therapy were small, as were the differences between the lobes of the prostate containing focal sites of uptake and those that were negative (fig. S19B). This is likely because RT-PCR reflects an average of the expression based on the whole lobe. However, immunopathology for regions with and without the ^{89}Zr-11B6 signal reveals subregions that continue to proliferate after treatment (fig. S20). Furthermore, the hK2 concentration in prostatic tissue

lysate indicated a strong positive correlation between ^{89}Zr-11B6 uptake and AR-dependent hK2 production (fig. S21).

Directing treatment in real-time

Radiolabeled and fluorescently labeled tracers indicated highly specific uptake in the cells of the prostate for noninvasive assessment (Fig. 3). To demonstrate the value of 11B6 imaging prostatic expression in the translational setting, we simulated the full treatment course encompassing pre-, intra-, and postoperative clinical decision points using dual-labeled ^{89}Zr-DFO and Cy5.5 for PET and fluorescence imaging. We explored this concept using the Pb_*KLK2*×Hi-*Myc* model.

PET was performed to assess disease burden (Fig. 7A), which was then resected using a fluorescent surgical stereoscope for real-time guidance (Fig. 7, B to G). Remnant prostatic tissue was harvested to confirm margins, and excised tissues were scanned for fluorescent and radio signals and hK2 protein (Fig. 7, H to J). After removing fluorescent tissues, the peritoneum and skin were sutured, and postoperative PET was acquired (Fig. 7K). A region of tracer accumulation could be identified by postoperative PET/CT imaging and was subsequently removed at autopsy. This was confirmed to be prostate tissue with fluorescence microscopy, autoradiography, and histochemistry (Fig. 7, L to N).

Humanized 11B6 and nonhuman primate toxicity

For intended use in humans, rodent CDRs were grafted into a human immunoglobulin framework to yield humanized 11B6 (hu11B6), without adverse effects on binding affinity or specificity. SPR-determined dissociation and association rate constants for all versions of 11B6 were calculated to be 10^{-5} (k_{off}) and 10^5 M^{-1} s^{-1} (k_{on}), respectively. No statistical difference in the apparent affinity was observed between hu11B6 and its DFO conjugate (fig. S2 and tables S1 to S3).

The kinetics and accumulation of the humanized conjugate ^{89}Zr-hu11B6 were not significantly different from the mouse IgG_1 version of 11B6 (fig. S22). Because humanization did not degrade affinity for the target or negate internalization of the immune complex, we proceeded to perform nonhuman primate testing. Male cynomolgus monkeys express hK2 detectable by 11B6, and therefore, we evaluated two of the monkeys in a dose-escalation study (weekly doses of 11B6, from 1.5, 3.0, 6.0, or 12.0 mg/kg). Body weight, hematology (blood cell counts, hemoglobin, and hematocrit), and serum chemistry (bilirubin, alanine aminotransferase, glucose phosphorus, and 11B6 concentration) were evaluated before the study and biweekly throughout. No mortality, behavioral changes, or toxicologically meaningful changes were observed (fig. S23). Finally, to assess the capacity to bind hK2 in human tissues, we applied 11B6 to human tissue specimens. The hK2 distribution in normal prostate, prostate adenocarcinoma, and a bone lesion can be identified by 11B6 immunodetection (fig. S24).

DISCUSSION

To improve PCa and TNBC management, we need the ability to detect malignant cells to monitor pathological processes or to deliver therapeutic compounds. Extracellular cytokines

and proteins are important mediators of these diseases, and they have been widely targeted with antibodies to combat disease or ameliorate its symptoms. However, biologics directed to these extracellular components have not enabled cellular targeting for imaging or treatment, limiting the ability to affect diseased cells themselves. Here, we demonstrate that an anti-hK2 antibody, 11B6, enables cell-specific accumulation in two common cancers for characterization, monitoring, and guidance.

Uptake of 11B6 in hK2-expressing tissues was FcRn-mediated, which is a demonstration of antibody-antigen internalization by cells in which they express the target. FcRn enables passive transfer of IgG from mother to offspring in the early stages of life and in a variety of physiologic functions in adult immunity. FcRn facilitates transport of IgG_1 and recycling of IgG immune complexes across otherwise impermeable polarized epithelia (23).11B6 exploits this mechanism, resulting in cellular accumulation of an immune complex, which avoids the precipitous washout observed using a previous kallikrein-targeted construct (15, 34). We demonstrate the wider applicability of this approach to enable cell-specific accumulation of a second SATA to PSA ($5A10^{H435\text{-}wt}$). FcRn binding is pH-dependent; the lower pH at sites of disease may provide an even more favorable microenvironment to generate imaging contrast compared to nonmalignant tissue. These results could be of importance for both PCa- and BCa-directed imaging and therapy and perhaps more widely as a strategy to improve both the magnitude and localization of internalizing SATA.

hK2 has traditionally been evaluated as a prostate biomarker; however, we have shown the uptake of ^{89}Zr-11B6 in AR-positive BCa xenografts under hormone stimulation. Questions surround the repercussions of AR status in BCa. Although several studies indicate a role for AR in pathways that negatively affect survival (35, 36), a correlation between AR and positive prognostic markers has also been identified (37, 38). The application of androgen antagonists in AR-positive BCa indicates that AR inhibition may be best directed toward basal (triple-negative) rather than luminal B-type/HER2 refractory subtypes (8, 35). Early trials suggest that this may represent a new approach to treat TNBC (8, 9). The 11B6 platform enables further study of the nuanced role of AR in the biology of BCa by offering the ability to guide and monitor treatment.

Here, we used several treatment methods in a range of models, aiming to eliminate long-standing impediments to noninvasive monitoring of disease biology and to assist development of AR-targeted therapies as a pharmacodynamic tool. In PCa and BCa disease assessment, biopsy is used to provide a direct readout of tissue organization but is restricted in time, access, and accuracy. The use of conventional imaging (ultrasound, CT, and MRI) to guide biopsy suffers from modest sensitivities for detection and staging (39, 40), with complication risks (41). If lesions are detectable, a direct biopsy can provide information on cellular processes but is invasive, costly, and difficult to repeat.

In contrast, ^{89}Zr-11B6 PET provides whole-body imaging of disease foci and a readout of AR activity for both primary and metastatic lesions. In a transgenic c-Myc-driven model of adenocarcinoma, we longitudinally evaluated AR activity during disease progression from the premalignant prostate through high disease burden. One limitation of the study of 11B6 in immunocompetent mice was the use of a single hK2-expressing disease-prone model.

Other PCa and BCa GEMM should be studied to assess the broad impact of the SATA approach. When this imaging platform was extended to evaluate treatment regimens, it revealed low levels of AR pathway reactivation at suborgan resolution and enabled a comparison between models of surgical castration and castration plus adjuvant therapy. The agent may also be used to guide treatment in real time or assist in treatment delivery (42, 43). ^{89}Zr-11B6 targets tumorous lesions themselves, rather than sites of remodeling, and is able to identify both osteoblastic and osteoclastic metastases. Conventional ^{18}F-NaF bone scans have high sensitivity but lack specificity for disease, confounding readout of burden especially after therapy. The enhanced precision of treatment monitoring by SATA will help to accelerate preclinical and translational research toward answering persistent questions for optimal patient care.

The technology presented here has direct application in both PCa and BCa patients. The humanized 11B6, which retains binding characteristics of the original agent and did not show adverse toxicological effects in nonhuman primates, is ready for clinical translation. Successful translation will have a broad and significant impact on individualized patient stratification and management at the molecular level. The approach to designing SATA that facilitates cellular uptake may be broadly relevant to detect, monitor, and treat a wide variety of diseases.

MATERIALS AND METHODS

Study design

The purpose of this study was to investigate the capacity of an antibody targeting the catalytically active site of a prostate-specific protease (in man) to delineate and guide treatment of primary and metastatic PCa and BCa. Binding properties and cellular interaction were evaluated in vitro and in vivo using fluorescent and radio conjugates. The internalization of this antibody, through the FcRn, after interaction with its secreted targeted antigen, was studied in detail. The same evaluation was also performed with a second antibody targeting another secreted antigen. Appending the positron-emitting zirconium-89 to the antibody for immunoPET was studied in subcutaneous, osseous, and hepatic metastatic models and in genetically engineered autochthonous PCa models. Tumor uptake and uptake kinetics were measured using manually defined regions of interest at multiple time points from 4 to 320 hours. Imaging studies in bone and GEMM systems were designed to measure treatment effect on AR activity with surgical and/or chemical castration. BCa cell lines were evaluated for *KLK2* expression and hK2 production with and without hormone stimulation. To study BCa hK2 production in vivo, we imaged BT474 xenografts with and without androgen stimulation by ^{89}Zr-11B6. Quantitative in vivo PET imaging data were assessed in addition to ex vivo autoradiography and gamma counting. PET study duration was sufficiently long to achieve 20×10^6 coincident events for low-noise reconstruction. Cohorts in treatment groups were randomized, and no outliers were excluded.

Reagents

All chemicals and biological assay agents were of the highest available purity and were purchased from Thermo Fisher Scientific, unless otherwise noted. Murine 11B6 was provided by K. Pettersson at the University of Turku, Finland, and hu11B6 was developed by Diaprost Inc. and produced by Innovagen Inc. Enzalutamide (MDV3100), which was manufactured by Medivation, was provided by C. Sawyers at the Memorial Sloan Kettering Cancer Center (MSKCC).

Preparation of zirconium-89

Zirconium-89 was produced through the $^{89}Y(p,n)^{89}Zr$ transmutation reaction on an EBCO TR19/9 variable beam energy cyclotron (Ebco Industries Inc.) in accordance with previously reported methods (44). ^{89}Zr-oxalate was isolated in high radionuclidic and radiochemical purity of >99.9% with an effective specific activity of 195 to 497 mega-becquerel (MBq)/μg (5.27 to 13.31 mCi/μg). Immediately before radiolabeling, ^{89}Zr[Zr]oxalate was neutralized with aliquots of 1 M $NaCO_3$ to pH 7.

Preparation of radiolabeled construct

Before conjugation, all antibodies were exchanged into 0.1 M Hepes (pH 8) by repeated ultracentrifugation (Amicon Centriplus YM-50, Millipore) and gel purification (PD10, GE Healthcare). The zirconium chelator, deferoxamine-*p*-SCN (AREVA Med), was conjugated to the antibody using a molar excess of 7:1. After addition of the bifunctional chelate, the reaction was adjusted to pH 8.5 with Na_2CO_3, shakenat 37°C for 1 hour, and then purified by repeated centrifugation, as above, into PBS. By isotopic dilution measurement, the average chelate/antibody ratio was determined to be 0.9 (45).

For radiolabeling, DFO-conjugated 11B6 (400 μl) was mixed with neutralized ^{89}Zr[Zr] and mixed gently. The pH after mixture was cross-checked and adjusted to pH 7, if needed. The labeling reaction was allowed to proceed for 1 hour. The conjugate was then purified by repeated purification by ultrafiltration into sterile saline. Radiochemical yield was assessed after purification; average yield was between 40 and 50%. Radiopurity was assessed by radio-instant thin layer chromatography. Briefly, ^{89}Zr-DFO-11B6 (^{89}Zr-11B6) was blotted (1 μl) on a silica-impregnated paper and eluted with a solution of 50 mM diethylenetriaminepentaacetic acid. All labeling reactions achieved >99% radiochemical purity. Average specific activity of the final radiolabeled conjugate was 1.4 mCi/mg.

Preparation of fluorescently labeled constructs

Before conjugation, all antibodies were purified as above. The near-infrared fluorophore Cy5.5-NHS (GE Healthcare) was resuspended in methanol, aliquoted, and dried by SpeedVac. Using a molar excess of 3:1, the antibody was labeled, and the pH was adjusted to 8.5 with Na_2CO_3. The reaction was shaken at 22°C for 4 hours, followed by gel purification (PD10) and ultrafiltration (Amicon). The number of dye molecules per antibody was evaluated using a spectrophotometer and calculated to be 1.3 (SpectraMax M5, Molecular Devices). The dyelabeled antibody conjugate was freshly prepared for each experiment.

Cell lines

LNCaP, DU-145, CWR22Rv1, MDAPCa2b, and VCaP were purchased from American Type Culture Collection (ATCC). The cell lines were cultured according to the manufacturer's instructions. LAPC4, LREX′, and LNCaP-AR/luc were previously developed and reported by the Sawyers laboratory (46–48).

Animal studies

All animal experiments were conducted in compliance with the institutional guidelines at the MSKCC. For xenograft studies, male athymic BALB/c (nu/nu) mice (6 to 8 weeks old, 20 to 25g) were obtained from Charles River Laboratories. LNCaP, DU-145, CWR22Rv1, MDAPCa2b, LAPC4, and VCaP tumors were inoculated in the right flank by subcutaneous injection of 1×10^6 to 5×10^6 cells in a 200-μl cell suspension of a 1:1 (v/v) mixture of medium with Matrigel (Collaborative Biomedical Products Inc.). Tumors developed after 3 to 7 weeks. Enzalutamide (MDV3100) was dissolved in dimethyl sulfoxide (DMSO) so that the final DMSO concentration when administered to animals would be ≤5%. The formulation of the vehicle is 1:0.1:5 (carboxymethyl cellulose/polysorbate 80/DMSO). Enzalutamide or vehicle was administered daily by gavage. Liver xenografts of the LREX′ line were implanted as described in the Supplementary Materials.

Flank xenografts of the BT474 cell line were established using previously described procedures (49). Briefly, 17β-estradiol pellets (0.72 mg per pellet) (Innovative Research of America) were inserted subcutaneously before inoculation of 1×10^6 cells in a 200-μl suspension of a 1:1 (v/v) mixture of medium with Matrigel (n =6).For this study, female Balb/c (nu/nu) animals were used. Animals in the DHT-positive group were supplemented with an additional subcutaneous 12.5 mg of DHT pellet (Innovative Research of America).

Preparation of osseous tumor grafts

Male CB-17 severe combined immunodeficient mice (6 to 8 weeks old) were anesthetized with a mixture of ketamine-xylazine, and a parapatellar incision was made in the left hindlimb. The tibia was punctured using a needle, and 1×10^5 cells (VCaP-luc or LNCaP-AR) were injected into the cavity. The puncture was closed with bone wax, the incision was sutured, and animals received a palliative dose of carprofen (5 mg/kg) once daily for 3 days after inoculation. Tumor development was followed with bioluminescence imaging and confirmed with CT.

Biodistribution studies

Biodistribution studies were conducted to evaluate the uptake of ^{89}Zr-11B6 in human PCa xenograft models. Mice received ^{89}Zr-11B6 [3.7 to 5.55 MBq (100 to 150 μCi); 300, 100, 50, or 15 μg of protein in 150 μl of sterile saline for injection] through intravenous tail vein injection (t = 0 hour). Animals (n = 4 to 5 per group) were euthanized by CO_2 asphyxiation at 24, 72, 96, 120, 240, and 344 hours after injection, and blood was immediately harvested by cardiac puncture. Eleven tissues (including the tumor) were removed, rinsed in water, dried on paper, weighed, and counted on a gamma counter for accumulation of ^{89}Zr radioactivity. Count data were corrected for background activity and decay, and the tissue

uptake (measured in units of %IA/g) for each sample was calculated by normalization to the total amount of activity injected.

Small animal PET imaging

PET imaging experiments were conducted on a microPET Focus 120 scanner (Concorde Microsystems). In initial studies, mice ($n \geq 4$) were administered with formulations of ^{89}Zr-11B6 [3.7 to 5.55 MBq (100 to 150 μCi); 300, 100, 50, or 25 μg of protein in 150 μl of sterile saline for injection] through tail vein injection. About 5 min before recording PET images, mice were anesthetized by inhalation of 1 to 2% isoflurane (Baxter Healthcare)/oxygen gas mixture and placed on the scanner bed. PET images were recorded at various time points between 1 and 344 hours after injection. List-mode data were acquired using a γ-ray energy window of 350 to 750 keV and a coincidence timing window of 6 ns. PET image data were corrected for detector non-uniformity, dead time, random coincidences, and physical decay. For all static images, scan time was adjusted to ensure that between 15 million and 25 million, coincident events were recorded.

Data were sorted into 3D histograms by Fourier rebinning, and transverse images were reconstructed using a maximum a priori algorithm to a 256 × 256 × 95 (0.72 mm × 0.72 mm × 1.3 mm) matrix. The reconstructed spatial resolution for zirconium-89 was 1.9 mm full-width half-maximum at the center of the field of view. The image data were normalized to correct for nonuniformity of response of the PET, dead-time count losses, positron branching ratio, and physical decay to the time of injection, but no attenuation, scatter, or partial volume averaging correction was applied. An empirically determined system calibration factor [in units of (mCi/ml)/(counts per second per voxel)] for mice was used to convert voxel count rates to activity concentrations. The resulting image data were then normalized to the administered activity to parameterize images in terms of %IA/g. Manually defined 3D regions of interest (also referred to as volumes of interest) were used to determine the maximum and mean %IA/g (decay corrected to the time of injection) in various tissues. Images were analyzed using the ASIPro VM software (Concorde Microsystems).

Small-animal CT imaging and coregistration

Animals that were scanned on both PET and x-ray CT systems were placed on a custom-built platform in a rigid body fixed position (using 0.1-mm polyethylene wrapping) (20). The bed was placed into an integrated heated air, anesthesia bed (MultiCell, Mediso). The bed was fixed in place on the microPET gantry and imaged as above. The bed was then moved for CT imaging using the NanoSPECT/CT (Bioscan). General acquisition parameters were 55 kVp with a pitch of 1 and 240 projections in a spiral scan mode. The entire animal was scanned using a multiple-field-of-view procedure (with an approximate field of view of 4 cm × 4 cm × 4 cm per bed position), commonly requiring three bed positions per scan. Total scan time was about 10 min. A Shepp-Logan filter was used during the reconstruction process to produce image matrices with isotropic volumes of 221 μm.

PET data were reconstructed using a 3D-filtered back projection maximum a priori algorithm using a ramp filter with a cutoff frequency equal to the Nyquist frequency into a 128 × 128 × 95 matrix (50). Data were exported in raw format, and the rigid body (three

degrees of freedom) coregistration between PET and CT data (and MRI, if applicable) was performed in Amira 5.3.3 (FEI). Amira and FIJI were used to produce most of the figures in the manuscript.

Fluorescence microscopy/surgical imaging/confocal microscopy

Micrographs were acquired using an Eclipse T*i* inverted microscope (Nikon) equipped with a motorized stage (Prior Scientific Instruments Ltd.), X-Cite light source (EXFO), and filter sets (Chroma). Images were acquired and processed using NIS-Elements (Nikon), FIJI (National Institutes of Health), and MosaicJ (Phillipe Thévenaz, Biomedical Imaging Group, Swiss Federal Institute of Technology Lausanne). All fluorescent images were captured with a fixed exposure time (fluorophore-dependent).

Confocal laser scanning microscopy used the TCS SP8 (Leica) in the Molecular Cytology Core Facility at the MSKCC. Cells were plated on glass bottom dishes (Nunc) for 48 hours, washed, and then incubated for the noted time with Cy5.5-IgG (control), Cy5.5-11B6, and/or excess blocking 11B6 in the supplemented medium. Samples were scanned for Cy5.5.

Cellular internalization assay

VCaP, LNCaP, and BT474 (with and without DHT stimulation) cells, cultured according to ATCC guidelines, were incubated with ^{89}Zr-11B6-containing medium. Uptake mechanism studies used purified human nonspecific IgG (400 μg per 1 ml per well, Invitrogen), human TruStain FcX Fc receptor blocking (40 μl per 1 ml per well, BioLegend), or h11B6 $(Fab')_2$ (0.2 mg per 1 ml per well, Diaprost Inc.) added together with the radioactive antibody. Control wells contained 20-fold excess of unlabeled antibody (to test specificity). Triplicate samples were periodically removed, and cells were washed with 1 ml of PBS (without Ca^{2+} and Mg^{2+} + 0.2% bovine serum albumin). Lysate generated (1 ml of 1 M NaOH for 5 min) was gamma-counted. Cell uptake was determined by calculating percent activity found in cell lysate [100 × (cell lysate activity/total activity)].

Confocal laser scanning microscopy was performed on cells beginning 12 hours after incubation with 1:200 of either Cy5.5-11B6, phAb-11B6 (Promega cat. no. G9841), or control Cy5.5-IgG. For FcRn colocalization, cells were fixed, permeabilized, and stained using anti-FcRn Alexa Fluor 488 (Thermo Fisher Scientific cat. no. NBP189128-FCGRT). FcRn is encoded by the *FCGRT* gene.

Affinity tests of ^{89}Zr-DFO-11B6, DFO-11B6 and, H435A-11B6

Biotinylated 11B6 (100 μl; 2 mg/liter) was added to streptavidin-coated microtiter plates, followed by 1 hour of incubation with shaking. The plate was washed and after which, 20, 100, 200, 400, or 1000 μg of compound (antibody) in 100 μl of DELFIA Assay Buffer was added to the wells, in duplicates, to compete with the capture antibody. Samples containing 0.34 or 3.4 ng/ml in 100 μl of DELFIA Assay Buffer were added hereafter to the wells. After 2-hour incubation with shaking, the plate was washed, and the europium (III) (Eu^{3+})–labeled tracer antibody 6H10 was added (200 μl; 0.5 mg/liter). The plate was incubated for 1

hour with shaking and then washed. DELFIA Enhancement Solution (200 μl) was added, and 5 min later, the time-resolved fluorescence was measured.

Time-resolved immunofluorometric assay of free and total hK2

Total hK2 was measured using an in-house research assay that has previously been described by Vaisänen *et al.*(17). Briefly, streptavidin-coated microtiter plates were incubated with the biotinylated catcher antibody 6H10, followed by washing and incubation with samples and standards. After another round of washing, the Eu^{3+}-labeled tracer antibody 7G1 was added. After incubation and washing steps, enhancement solution was added before reading the plates. Free hK2 was measured in a similar fashion, with biotin-labeled 11B6 as a capture antibody and Eu^{3+}-labeled 6H10 as a tracer antibody. Both assays have a functional detection limit of 0.04 ng/ml.

Tissue lysate preparation and total protein measurement

Prostate tissues harvested from transgenic mice were homogenized in lysis buffer [50 mM sodium acetate, 2 mM EDTA, 1% Triton X-100, 1× complete protease inhibitor (Roche), and 10 mM benzamidine], sonicated for 10 s (550 Sonic Dismembrator, Thermo Fisher Scientific), and centrifuged at 13,000 rpm for 10 min. The supernatant was saved for measurement of free and total hK2. Total protein concentrations were determined in homogenates using the Bio-Rad DC Protein Assay. Details of the generation of GEMM can be found in the Supplementary Materials.

RNA isolation and quantitative PCR

About 200 mm^3 of tumor sample was placed in a FastPrep Lysing Matrix tube (MP Biomedicals). Tumors were then homogenized in 500 μl of TRIzol (Ambion) using a FastPrep-24 instrument (MP Biomedicals). For xenograft tumors, the samples were transferred to a new Eppendorf tube, where 100 μg of glycogen (Ambion) was added. The samples were mixed by inversion and allowed to sit at room temperature for 5 min. Chloroform (100 μl; OmniSolv) was added, and the samples were shaken vigorously and incubated for 3 min. The samples were then centrifuged at 11,500 rpm at 4°C for 15 min, and the aqueous (top) phase was transferred to a new Eppendorf tube. Isopropanol (250 μl) was added to the sample by pipetting until a precipitate formed. The sample was then centrifuged at 11,500 rpm at 4°C for 10 min. The pellet was washed with 75 to 80% EtOH in diethyl pyrocarbonate water (Ambion). RNA was then purified using the RNeasy Mini Kit (Qiagen) or the PureLink RNA Mini Kit (Ambion). RNA quality and quantity were determined using a spectrophotometer at 260 and 280 nm (Nanodrop 2000, Thermo Fisher Scientific). Complementary DNA (cDNA) was generated using the High-Capacity cDNA Reverse Transcription Kit (Applied Biosystems, Life Technologies). Quantitative PCR was done using QuantiFast SYBR Green PCR Kit and RT^2 qPCR primers (Qiagen) on a $RealPlex^4$ MasterCycler system (Eppendorf). KLK2 expression was quantified relative to β-actin using the comparative CT method.

Single-cell extractions of prostatic tissue

A suspension of single cells was derived from the excised mouse prostatic tissue (of animals dosed with 100 μg of Cy5.5-11B6) by mincing the tissue at 4°C, digesting it for 3 hours in collagenase/hyaluronidase (STEMCELL Technologies) in culture medium (Dulbecco's modified Eagle's medium with 5% fetal bovine serum) at 37°C, and incubating it in trypsin for 1 hour at 4°C, followed by low-speed centrifugation. The cell pellet was resuspended in dispase (5 mg/ml) and deoxyribonuclease I (1 mg/ml) (STEMCELL Technologies) and pipetted gently before being passed through a 70-μm strainer (Thermo Fisher Scientific). Aliquots of the suspension were placed between two glass coverslips and scanned on the Eclipse T*i*, as previously described.

Statistical analysis

Data are presented as means ± SEM, unless otherwise noted. Statistical significance was analyzed by nonparametric Student's *t* test. Pearson's correlation coefficients were used for assessing the strength of association between pairs of predefined variables. In all cases, differences in results were considered to be statistically significant when the computed *P* value was less than 0.05. All tests were two-tailed. Analyses were performed using Prism 6.0 (GraphPad).

Supplementary Material

Refer to Web version on PubMed Central for supplementary material.

Acknowledgments

We thank M. R. McDevitt, P. W. Kantoff, and D. A. Scheinberg of the Memorial Sloan Kettering Cancer Center (MSKCC) and J. V. Ravetch of the Rockefeller University for intellectual input; C. Sawyers and his laboratory at the MSKCC for providing scientific contributions and enzalutamide; and K. Pettersson at the University of Turku, Finland for providing reagents. We thank the following members of the MSKCC Small-Animal Imaging Core Facility for technical support and expertise: P. Zanzonico, director, B. J. Beattie, and M. Lupu.

Funding: This study was supported in part by the NIH [grants P30 CA008748 (MSKCC Cancer Center Support Grant) and P30 CA006973 (Johns Hopkins University Cancer Center Support Grant)]. The MSKCC Small-Animal Imaging Core Facility is supported in part by the NIH (grants P30 CA008748-48, S10 RR020892-01, and S10 RR028889-01) and the Geoffrey Beene Cancer Research Center. We also acknowledge W. H. Goodwin and A. Goodwin and their Commonwealth Foundation for Cancer Research, the Experimental Therapeutics Center, and the Radiochemistry and Molecular Imaging Probe Core (P50-CA086438); all of MSKCC. D.L.J.T. was supported by the NIH Molecular Imaging Fellowship Program (5R25CA096945-07) and the Steve Wynn Prostate Cancer Foundation Young Investigator Award (PCF-YIA). D.U. was supported in part by the Knut and Alice Wallenberg Foundation, the Bertha Kamprad Foundation, and the David H. Koch PCF-YIA. S.M.L. was supported by the Ludwig Center for Cancer Immunotherapy at the MSKCC and the National Cancer Institute (P50-CA86438); S.-E.S. by the Swedish Cancer Society and the Swedish National Health Foundation (Avtal om Läkarutbildning); H.L. was supported in part by the National Cancer Institute (R33 CA127768-02), the National Institute for Health Research (NIHR) Oxford Biomedical Research Centre program, the Swedish Cancer Society(3455,14-0722),and the Swedish Research Council(Medicine-20095). P.T.S., H.I.S., and H.L. were supported in part by the MSKCC Specialized Programs of Research Excellence in Prostate Cancer (P50CA92629),the David H. Koch Fund of the PCF, and the Sidney Kimmel Center for Prostate and Urologic Cancers. D.V. was supported in part by the Hascoe Charitable Foundation.

REFERENCES AND NOTES

1. Wong YN, Ferraldeschi R, Attard G, de Bono J. Evolution of androgen receptor targeted therapy for advanced prostate cancer. Nat Rev Clin Oncol. 2014; 11:365–376. [PubMed: 24840076]

2. Visakorpi T, Hyytinen E, Koivisto P, Tanner M, Keinanen R, Palmberg C, Palotie A, Tammela T, Isola J, Kallioniemi OP. In vivo amplification of the androgen receptor gene and progression of human prostate cancer. Nat Genet. 1995; 9:401–406. [PubMed: 7795646]

3. Titus MA, Schell MJ, Lih FB, Tomer KB, Mohler JL. Testosterone and dihydrotestosterone tissue levels in recurrent prostate cancer. Clin Cancer Res. 2005; 11:4653–4657. [PubMed: 16000557]

4. Mellinghoff IK, Vivanco I, Kwon A, Tran C, Wongvipat J, Sawyers CL. HER2/neu kinase-dependent modulation of androgen receptor function through effects on DNA binding and stability. Cancer Cell. 2004; 6:517–527. [PubMed: 15542435]

5. Niemeier LA, Dabbs DJ, Beriwal S, Striebel JM, Bhargava R. Androgen receptor in breast cancer: Expression in estrogen receptor-positive tumors and in estrogen receptor-negative tumors with apocrine differentiation. Mod Pathol. 2010; 23:205–212. [PubMed: 19898421]

6. Santagata S, Thakkar A, Ergonul A, Wang B, Woo T, Hu R, Harrell JC, McNamara G, Schwede M, Culhane AC, Kindelberger D, Rodig S, Richardson A, Schnitt SJ, Tamimi RM, Ince TA. Taxonomy of breast cancer based on normal cell phenotype predicts outcome. J Clin Invest. 2014; 124:859–870. [PubMed: 24463450]

7. Choi JE, Kang SH, Lee SJ, Bae YK. Androgen receptor expression predicts decreased survival in early stage triple-negative breast cancer. Ann Surg Oncol. 2015; 22:82–89. [PubMed: 25145503]

8. Gucalp A, Tolaney S, Isakoff SJ, Ingle JN, Liu MC, Carey LA, Blackwell K, Rugo H, Nabell L, Forero A, Stearns V, Doane AS, Danso M, Moynahan ME, Momen LF, Gonzalez JM, Akhtar A, Giri DD, Patil S, Feigin KN, Hudis CA, Traina TA. Translational Breast Cancer Research Consortium, Phase II trial of bicalutamide in patients with androgen receptor-positive, estrogen receptor-negative metastatic breast cancer. Clin Cancer Res. 2013; 19:5505–5512. [PubMed: 23965901]

9. Arce-Salinas C, Riesco-Martinez MC, Hanna W, Bedard P, Warner E. Complete response of metastatic androgen receptor-positive breast cancer to bicalutamide: Case report and review of the literature. J Clin Oncol. 2014; 34:e21–e24. [PubMed: 24888812]

10. Diabetic Retinopathy Clinical Research Network. Wells JA, Glassman AR, Ayala AR, Jampol LM, Aiello LP, Antoszyk AN, Arnold-Bush B, Baker CW, Bressler NM, Browning DJ, Elman MJ, Ferris FL, Friedman SM, Melia M, Pieramici DJ, Sun JK, Beck RW. Aflibercept, bevacizumab, or ranibizumab for diabetic macular edema. N Engl J Med. 2015; 372:1193–1203. [PubMed: 25692915]

11. Yang JC, Haworth L, Sherry RM, Hwu P, Schwartzentruber DJ, Topalian SL, Steinberg SM, Chen HX, Rosenberg SA. A randomized trial of bevacizumab, an anti-vascular endothelial growth factor antibody, for metastatic renal cancer. N Engl J Med. 2003; 349:427–434. [PubMed: 12890841]

12. Cummings SR, San Martin J, McClung MR, Siris ES, Eastell R, Reid IR, Delmas P, Zoog HB, Austin M, Wang A, Kutilek S, Adami S, Zanchetta J, Libanati C, Siddhanti S, Christiansen C, FREEDOM Trial. Denosumab for prevention of fractures in postmenopausal women with osteoporosis. N Engl J Med. 2009; 361:756–765. [PubMed: 19671655]

13. Croft M, Benedict CA, Ware CF. Clinical targeting of the TNF and TNFR superfamilies. Nat Rev Drug Discov. 2013; 12:147–168. [PubMed: 23334208]

14. Nagengast WB, Lub-de Hooge MN, Oosting SF, den Dunnen WF, Warnders F-J, Brouwers AH, de Jong JR, Price PM, Hollema H, Hospers GA, Elsinga PH, Hesselink JW, Gietema JA, de Vries EG. VEGF-PET imaging is a noninvasive biomarker showing differential changes in the tumor during sunitinib treatment. Cancer Res. 2011; 71:143–153. [PubMed: 21084271]

15. Ulmert D, Evans MJ, Holland JP, Rice SL, Wongvipat J, Pettersson K, Abrahamsson PA, Scardino PT, Larson SM, Lilja H, Lewis JS, Sawyers CL. Imaging androgen receptor signaling with a radiotracer targeting free prostate-specific antigen. Cancer Discov. 2012; 2:320–327. [PubMed: 22576209]

16. Thorek DLJ, Evans MJ, Carlsson SV, Ulmert D, Lilja H. Prostate-specific kallikrein-related peptidases and their relation to prostate cancer biology and detection. Established relevance and emerging roles. Thromb Haemost. 2013; 110:484–492. [PubMed: 23903407]

17. Vaisänen V, Eriksson S, Ivaska KK, Lilja H, Nurmi M, Pettersson K. Development of sensitive immunoassays for free and total human glandular kallikrein 2. Clin Chem. 2004; 50:1607–1617. [PubMed: 15247158]

18. Choe YS, Lidstrom PJ, Chi DY, Bonasera TA, Welch MJ, Katzenellenbogen JA. Synthesis of 11β-[^{18}F]fluoro-5α-dihydrotestosterone and 11β-[^{18}F]fluoro-19-nor-5α-dihydrotestosterone: Preparation via halofluorination-reduction, receptor binding, and tissue distribution. J Med Chem. 1995; 38:816–825. [PubMed: 7877147]
19. Scher HI, Beer TM, Higano CS, Anand A, Taplin ME, Efstathiou E, Rathkopf D, Shelkey J, Yu EY, Alumkal J, Hung D, Hirmand M, Seely L, Morris MJ, Danila DC, Humm J, Larson S, Fleisher M, Sawyers CL. Prostate Cancer Foundation/Department of Defense Prostate Cancer Clinical Trials Consortium, Antitumour activity of MDV3100 in castration-resistant prostate cancer: A phase 1-2study. Lancet. 2010; 375:1437–1446. [PubMed: 20398925]
20. Beattie BJ, Forster GJ, Govantes R, Le CH, Longo VA, Zanzonico PB, Bidaut L, Blasberg RG, Koutcher JA. Multimodality registration without a dedicated multimodality scanner. Mol Imaging. 2007; 6:108–120. [PubMed: 17445505]
21. Even-Sapir E, Metser U, Mishani E, Lievshitz G, Lerman H, Leibovitch I. The detection of bone metastases in patients with high-risk prostate cancer: ^{99m}Tc-MDP planar bone scintigraphy, single- and multi-field-of-view SPECT, ^{18}F-fluoride PET, and ^{18}F-fluoride PET/CT. J Nucl Med. 2006; 47:287–297. [PubMed: 16455635]
22. Ulmert D, Solnes L, Thorek D. Contemporary approaches for imaging skeletal metastasis. Bone Res. 2015; 3:15024. [PubMed: 26273541]
23. Yoshida M, Claypool SM, Wagner JS, Mizoguchi E, Mizoguchi A, Roopenian DC, Lencer WI, Blumberg RS. Human neonatal Fc receptor mediates transport of IgG into luminal secretions for delivery of antigens to mucosal dendritic cells. Immunity. 2004; 20:769–783. [PubMed: 15189741]
24. Firan M, Bawdon R, Radu C, Ober RJ, Eaken D, Antohe F, Ghetie V, Ward ES. The MHC class I-related receptor, FcRn, plays an essential role in the maternofetal transfer of γ-globulin in humans. Int Immunol. 2001; 13:993–1002. [PubMed: 11470769]
25. Raghavan M, Bonagura VR, Morrison SL, Bjorkman PJ. Analysis of the pH dependence of the neonatal Fc receptor/immunoglobulin G interaction using antibody and receptor variants. Biochemistry. 1995; 34:14649–14657. [PubMed: 7578107]
26. Tannock IF, Rotin D. Acid pH in tumors and its potential for therapeutic exploitation. Cancer Res. 1989; 49:4373–4384. [PubMed: 2545340]
27. Ellwood-Yen K, Graeber TG, Wongvipat J, Iruela-Arispe ML, Zhang J, Matusik R, Thomas GV, Sawyers CL. Myc-driven murine prostate cancer shares molecular features with human prostate tumors. Cancer Cell. 2003; 4:223–238. [PubMed: 14522256]
28. Roopenian DC, Akilesh S. FcRn: The neonatal Fc receptor comes of age. Nat Rev Immunol. 2007; 7:715–725. [PubMed: 17703228]
29. Ober RJ, Radu CG, Ghetie V, Ward ES. Differences in promiscuity for antibody-FcRn interactions across species: Implications for therapeutic antibodies. Int Immunol. 2001; 13:1551–1559. [PubMed: 11717196]
30. Magklara A, Grass L, Diamandis EP. Differential steroid hormone regulation of human glandular kallikrein (hK2) and prostate-specific antigen (PSA) in breast cancer cell lines. Breast Cancer Res Treat. 2000; 59:263–270. [PubMed: 10832596]
31. Black MH, Magklara A, Obiezu C, Levesque MA, Sutherland DJ, Tindall DJ, Young CY, Sauter ER, Diamandis EP. Expression of a prostate-associated protein, human glandular kallikrein (hK2), in breast tumours and in normal breast secretions. Br J Cancer. 2000; 82:361–367. [PubMed: 10646889]
32. Giai M, Yu H, Roagna R, Ponzone R, Katsaros D, Levesque MA, Diamandis EP. Prostate-specific antigen in serum of women with breast cancer. Br J Cancer. 1995; 72:728–731. [PubMed: 7545417]
33. Hussain M, Tangen CM, Berry DL, Higano CS, Crawford ED, Liu G, Wilding G, Prescott S, Kanaga Sundaram S, Small EJ, Dawson NA, Donnelly BJ, Venner PM, Vaishampayan UN, Schellhammer PF, Quinn DI, Raghavan D, Ely B, Moinpour CM, Vogelzang NJ, Thompson IM Jr. Intermittent versus continuous androgen deprivation in prostate cancer. N Engl J Med. 2013; 368:1314–1325. [PubMed: 23550669]

34. Evans-Axelsson S, Ulmert D, Orbom A, Peterson P, Nilsson O, Wennerberg J, Strand J, Wingardh K, Olsson T, Hagman Z, Tolmachev V, Bjartell A, Lilja H, Strand SE. Targeting free prostate-specific antigen for in vivo imaging of prostate cancer using a monoclonal antibody specific for unique epitopes accessible on free prostate-specific antigen alone. Cancer Biother Radiopharm. 2012; 27:243–251. [PubMed: 22489659]

35. Ni M, Chen Y, Lim E, Wimberly H, Bailey ST, Imai Y, Rimm DL, Liu XS, Brown M. Targeting androgen receptor in estrogen receptor-negative breast cancer. Cancer Cell. 2011; 20:119–131. [PubMed: 21741601]

36. Robinson JLL, Macarthur S, Ross-Innes CS, Tilley WD, Neal DE, Mills IG, Carroll JS. Androgen receptor driven transcription in molecular apocrine breast cancer is mediated by FoxA1. EMBO J. 2011; 30:3019–3027. [PubMed: 21701558]

37. Lehmann BD, Bauer JA, Chen X, Sanders ME, Chakravarthy AB, Shyr Y, Pietenpol JA. Identification of human triple-negative breast cancer subtypes and preclinical models for selection of targeted therapies. J Clin Invest. 2011; 121:2750–2767. [PubMed: 21633166]

38. Rakha EA, El-Sayed ME, Green AR, Lee AH, Robertson JF, Ellis IO. Prognostic markers in triple-negative breast cancer. Cancer. 2007; 109:25–32. [PubMed: 17146782]

39. Vo T, Rifkin MD, Peters TL. Should ultrasound criteria of the prostate be redefined to better evaluate when and where to biopsy. Ultrasound Q. 2001; 17:171–176. [PubMed: 12973073]

40. Wu LM, Xu JR, Ye YQ, Lu Q, Hu JN. The clinical value of diffusion-weighted imaging in combination with T2-weighted imaging in diagnosing prostate carcinoma: A systematic review and meta-analysis. AJR Am J Roentgenol. 2012; 199:103–110. [PubMed: 22733900]

41. Loeb S, Carter HB, Berndt SI, Ricker W, Schaeffer EM. Complications after prostate biopsy: Data from SEER-Medicare. J Urol. 2011; 186:1830–1834. [PubMed: 21944136]

42. Vilhelmsson Timmermand O, Larsson E, Ulmert D, Tran TA, Strand S. Radioimmunotherapy of prostate cancer targeting human kallikrein-related peptidase 2. EJNMMI Res. 2016; 6:27. [PubMed: 26983637]

43. Timmermand OV, Tran TA, Strand SE, Axelsson J. Intratherapeutic biokinetic measurements, dosimetry parameter estimates, and monitoring of treatment efficacy using cerenkov luminescence imaging in preclinical radionuclide therapy. J Nucl Med. 2015; 56:444–449. [PubMed: 25655628]

44. Holland JP, Sheh Y, Lewis JS. Standardized methods for the production of high specific-activity zirconium-89. Nucl Med Biol. 2009; 36:729–739. [PubMed: 19720285]

45. Holland JP, Divilov V, Bander NH, Smith-Jones PM, Larson SM, Lewis JS. ^{89}Zr-DFO-J591 for immunoPET of prostate-specific membrane antigen expression in vivo. J Nucl Med. 2010; 51:1293–1300. [PubMed: 20660376]

46. Chen CD, Welsbie DS, Tran C, Baek SH, Chen R, Vessella R, Rosenfeld MG, Sawyers CL. Molecular determinants of resistance to antiandrogen therapy. Nat Med. 2004; 10:33–39. [PubMed: 14702632]

47. Arora VK, Schenkein E, Murali R, Subudhi SK, Wongvipat J, Balbas MD, Shah N, Cai L, Efstathiou E, Logothetis C, Zheng D, Sawyers CL. Glucocorticoid receptor confers resistance to antiandrogens by bypassing androgen receptor blockade. Cell. 2013; 155:1309–1322. [PubMed: 24315100]

48. Tran C, Ouk S, Clegg NJ, Chen Y, Watson PA, Arora V, Wongvipat J, Smith-Jones PM, Yoo D, Kwon A, Wasielewska T, Welsbie D, Chen CD, Higano CS, Beer TM, Hung DT, Scher HI, Jung ME, Sawyers CL. Development of a second-generation antiandrogen for treatment of advanced prostate cancer. Science. 2009; 324:787–790. [PubMed: 19359544]

49. She QB, Chandarlapaty S, Ye Q, Lobo J, Haskell KM, Leander KR, DeFeo-Jones D, Huber HE, Rosen N. Breast tumor cells with *PI3K* mutation or *HER2* amplification are selectively addicted to Akt signaling. PLOS ONE. 2008; 3:e3065. [PubMed: 18725974]

50. Qi J, Leahy RM, Cherry SR, Chatziioannou A, Farquhar TH. High-resolution 3D Bayesian image reconstruction using the microPET small-animal scanner. Phys Med Biol. 1998; 43:1001–1013. [PubMed: 9572523]

51. Kilpinen S, Autio R, Ojala K, Iljin K, Bucher E, Sara H, Pisto T, Saarela M, Skotheim RI, Bjorkman M, Mpindi JP, Haapa-Paananen S, Vainio P, Edgren H, Wolf M, Astola J, Nees M, Hautaniemi S, Kallioniemi O. Systematic bioinformatic analysis of expression levels of 17,330

human genes across 9,783 samples from 175 types of healthy and pathological tissues. Genome Biol. 2008; 9:R139. [PubMed: 18803840]

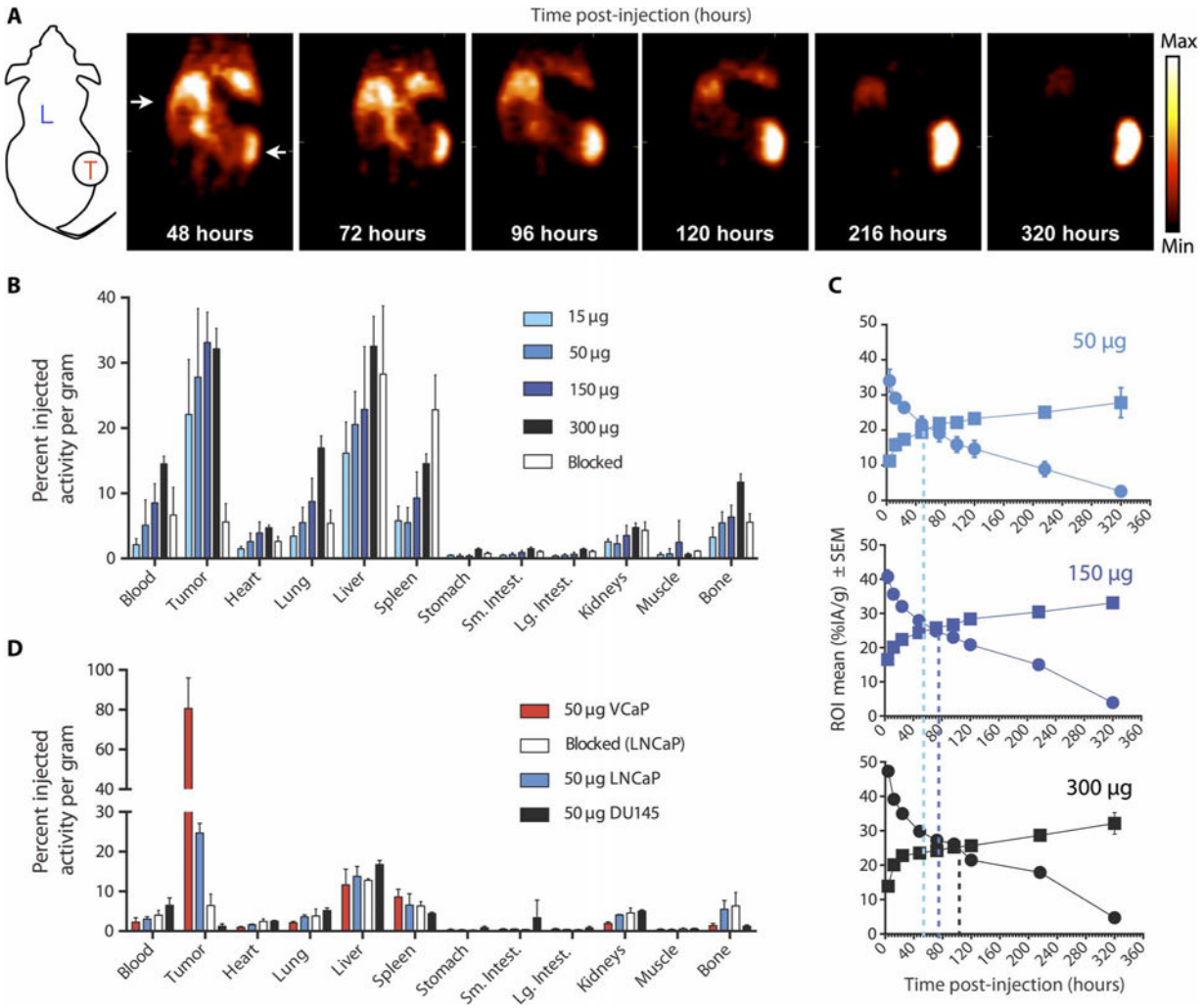

Fig. 1. 11B6 immunoPET imaging of PCa

(A) Coronal slices through xenograft (LNCaP)-bearing mice over time. The long-lived PET isotope ^{89}Zr enables longitudinal imaging, which shows continued uptake over 10 days. Schematic shows liver (L) and location of tumor (T) on flank. (**B** and **C**) Ex vivo determination (B) of organ and tumor antibody distribution at 320 hours, with time activity curves (C) in %IA/g of tumor (squares) and blood (circles) for 50-, 150-, and 300-µg doses (top to bottom). **(D)** Greater uptake in the higher hk2-producing VCaP in comparison to the LNCaP and nonproducing DU145 xenografts indicates specificity, which can also be blocked with cold antibody (1 mg). ROI, region of interest.

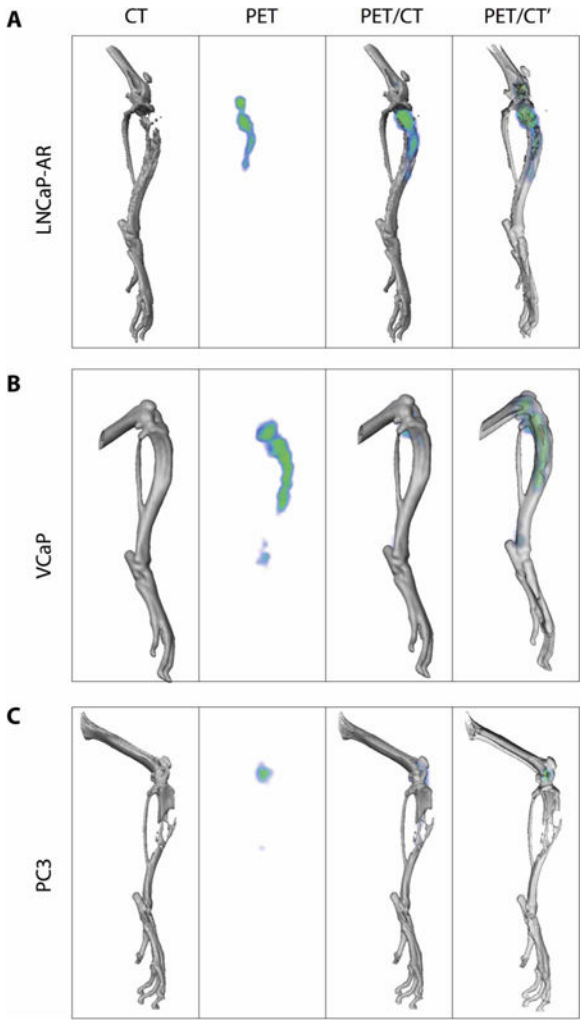

Fig. 2. Precision imaging of metastatic lesions

^{89}Zr-DFO-11B6 delineates osteolytic and osteoblastic bone metastases. (**A** and **B**) The radiotracer is able to distinguish both LNCaP-AR osteolytic (A) and VCaP osteoblastic (B) tumors. (**C**) PC3 AR- and hK2-negative osteolytic lesions in the mouse tibia. X-ray computed tomography (CT) (leftmost column) of the electron-dense bone shows the loss of bone in the LNCaP and PC3 models. The intensity of signal recapitulates the relative hK2 expression in the two AR-positive cell lines (PET column, second from left). Three-dimensional (3D) PET/CT fusion images with opaque bone (second column from right) and transparent bone (rightmost column) show that these metastases are restricted from the surrounding soft tissue. Low amounts of nonspecific ^{89}Zr uptake at the epiphyseal growth plate are seen in all models.

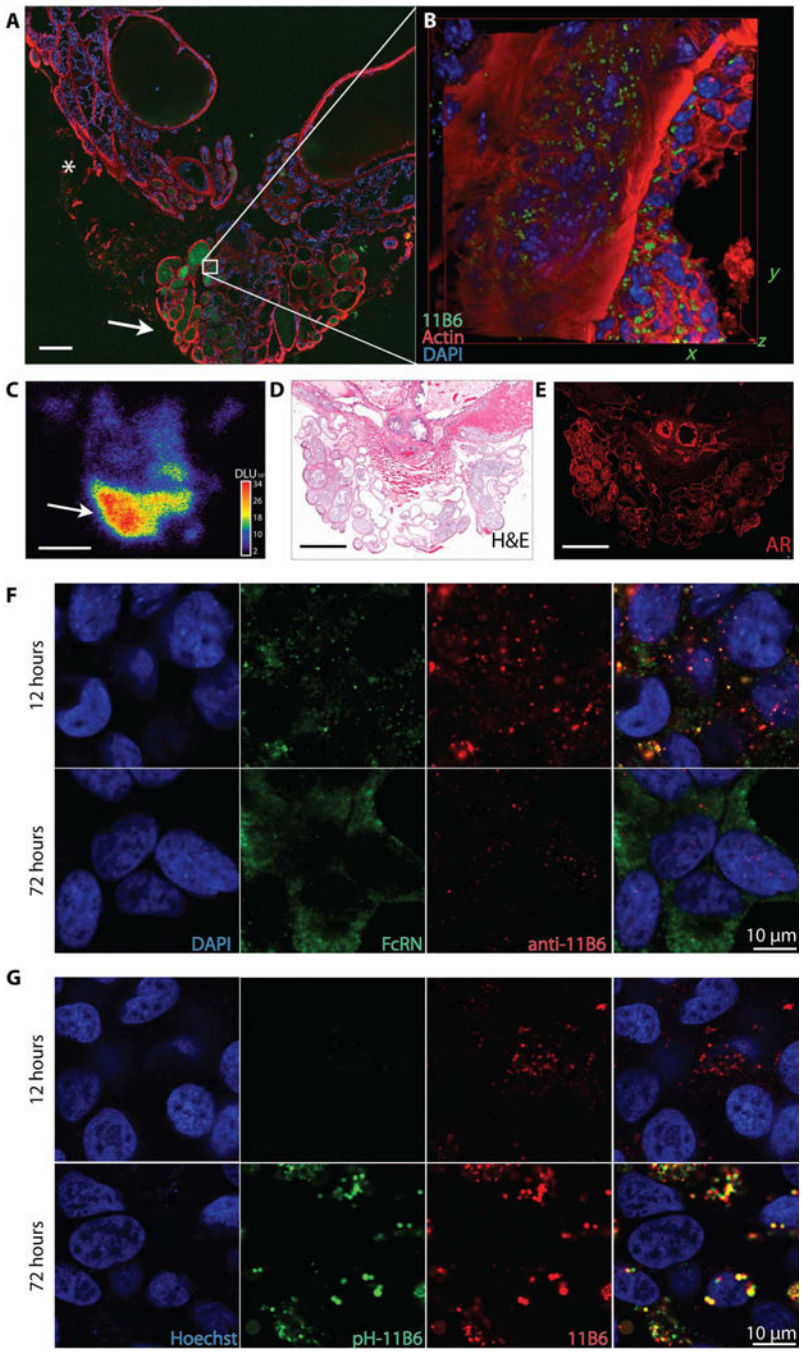

Fig. 3. Intracellular accumulation of 11B6-hK2

The neonatal receptor facilitates internalization of the anti-hK2 immunocomplex. (**A** to **C**) The whole prostate and seminal vesicles (prostate package) were removed from Pb_KLK2 mice 72 hours after injection of Cy5.5-11B6 and ^{89}Zr-11 B6 for whole-mount fluorescence (A), inset box volume scanned by confocal microscopy (B), and whole-mount autoradiography (C). Intense uptake was seen in the glandular structures of the ventral prostate (arrow), with lower uptake in the dorsolateral prostate (*). DAPI, 4′,6-diamidino-2-phenylindole; DLU, digital light units. **(D)** Radio and fluorescent signals in glands of the

ventral prostate were localized by anatomical staining with hematoxylin and eosin (H&E). **(E)** AR staining is intense in the ventral prostate. Scale bar, 500 μm. (**F** and **G**) After incubation with LNCaP PCa cells, the 11B6 antibody colo-calizes with FcRn early (F) and is then trafficked to acidified lysosomes (G), as indicated by increased fluorescence from pH-responsive dye-labeled 11B6 (pH-11B6).

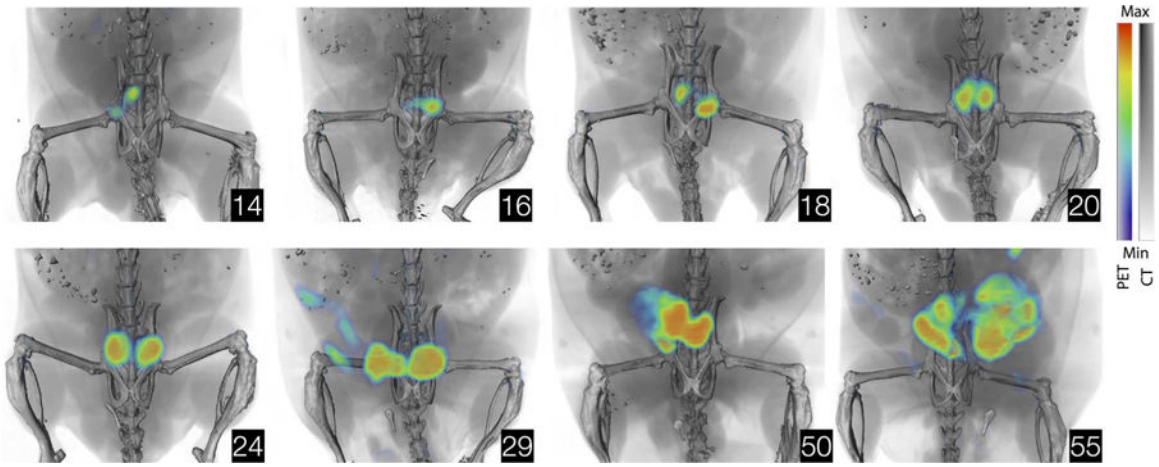

Fig. 4. Imaging cancer development

Noninvasive annotation of PCa development by ^{89}Zr-11B6. Representative ^{89}Zr-11B6 (50 μg) PET/CT images of cancer-susceptible hK2-expressing mice (Pb_*KLK2* × Hi-*Myc*) throughout development of adenocarcinoma. Inserts display age in weeks.

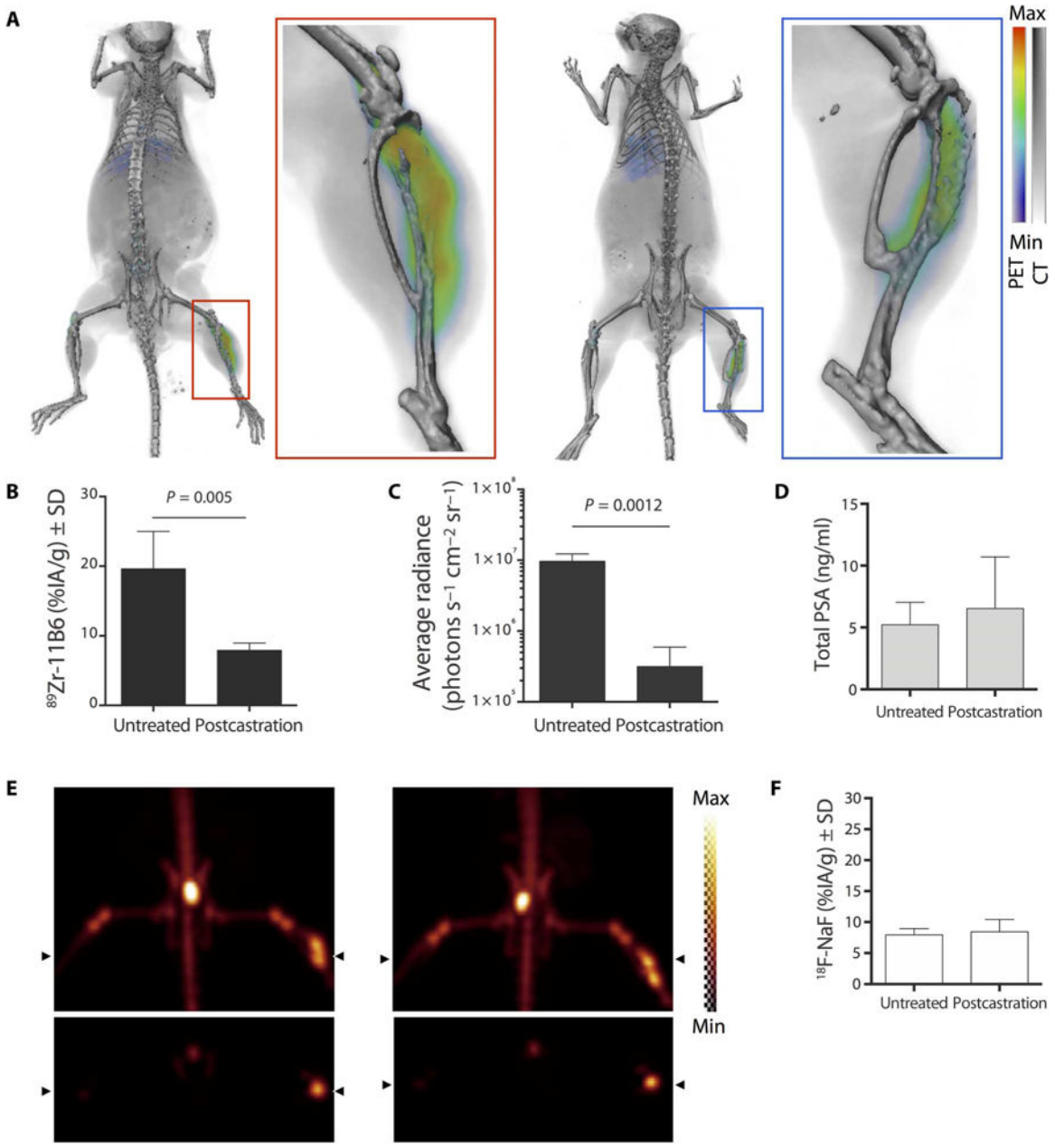

Fig. 5. Lesion response to treatment

(A) Representative PET imaging with ^{89}Zr-11B6 on an intraosseous LNCaP-AR model before (left) and after (right) castration. **(B** and **C)** Quantification of imaging results of ^{89}Zr-11B6 radiotracer uptake (B) reflects AR-driven luciferase (C) signal changes in the LNCaP-AR cell line. **(D)** In contrast, PSA blood concentration values remained unchanged. (**E**) Conventional ^{18}F-NaF imaging was also conducted before (left) and after (right) castration before providing ^{89}Zr-11B6. **(F)** Quantitation of bone scan uptake values illustrates continued bone turnover at the site of the resolved lesion. $n = 5$ per group for imaging experiments, and $n = 4$ per group for PSA assay (table S6).

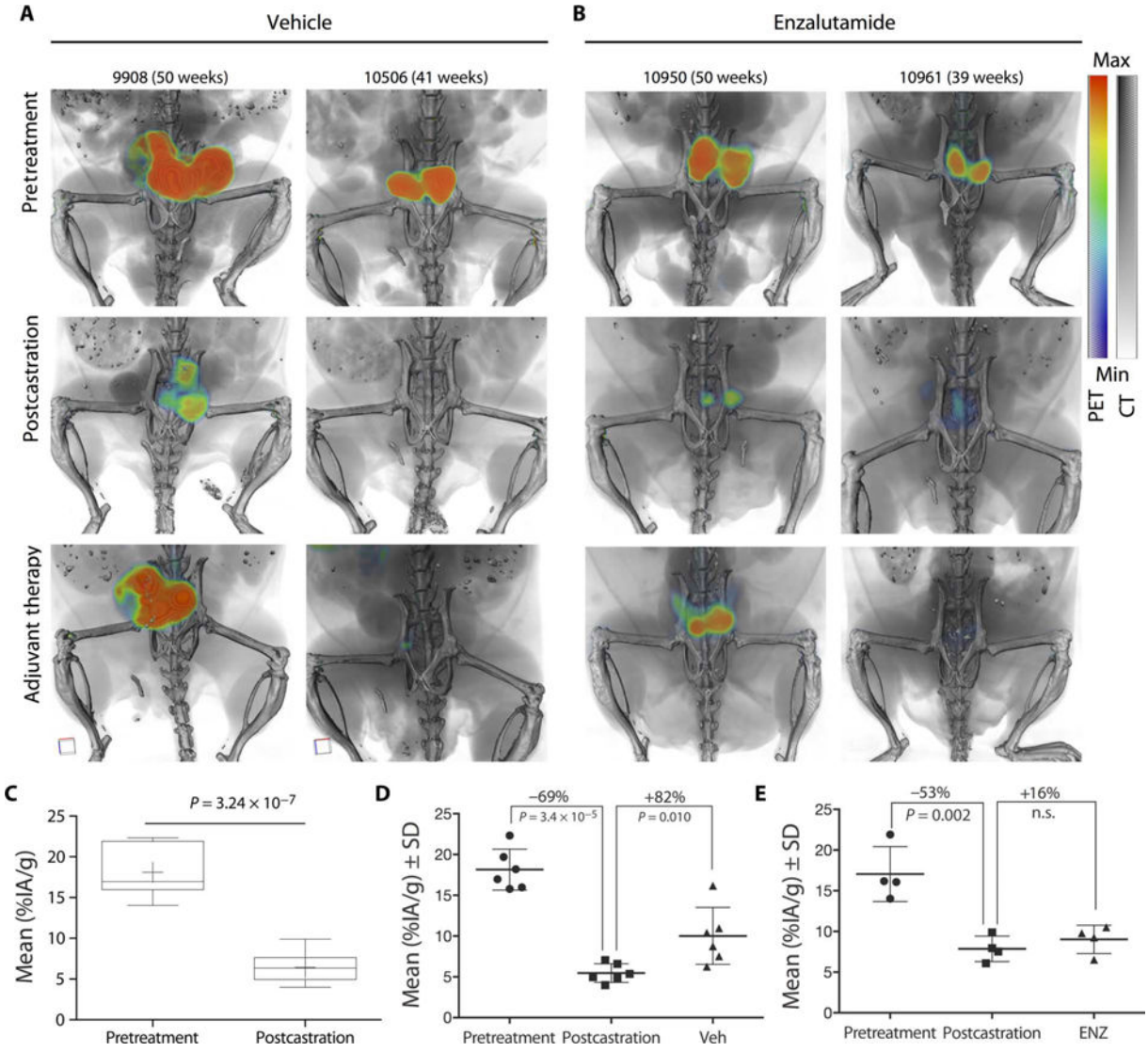

Fig. 6. Characterization of drug response to surgical castration and adjuvant AR blockade

Noninvasive longitudinal quantification of castration and anti-androgen therapy with ^{89}Zr-11B6. Pb_*KLK2* × Hi-*Myc* mice were imaged before treatment, after castration (6 weeks after surgery), and after adjuvant therapeutic intervention [4 weeks after either vehicle or enzalutamide (ENZ)]. **(A** and **B)** Two representative animals from the vehicle [phosphate-buffered saline (PBS)] (A) and enzalutamide (B) treatment groups are shown. **(C)** Quantification (mean %IA/g) of ^{89}Zr-11B6 targeting in groups, before surgery (n =14) and after castration (n = 10). **(D** and **E)** Mean uptake in the vehicle (Veh) (n =6) (D) and enzalutamide (n = 4) (E) groups through the entire adjuvant treatment regimen. Reactivation in the castration plus AR blockade group was not significant (n.s.).

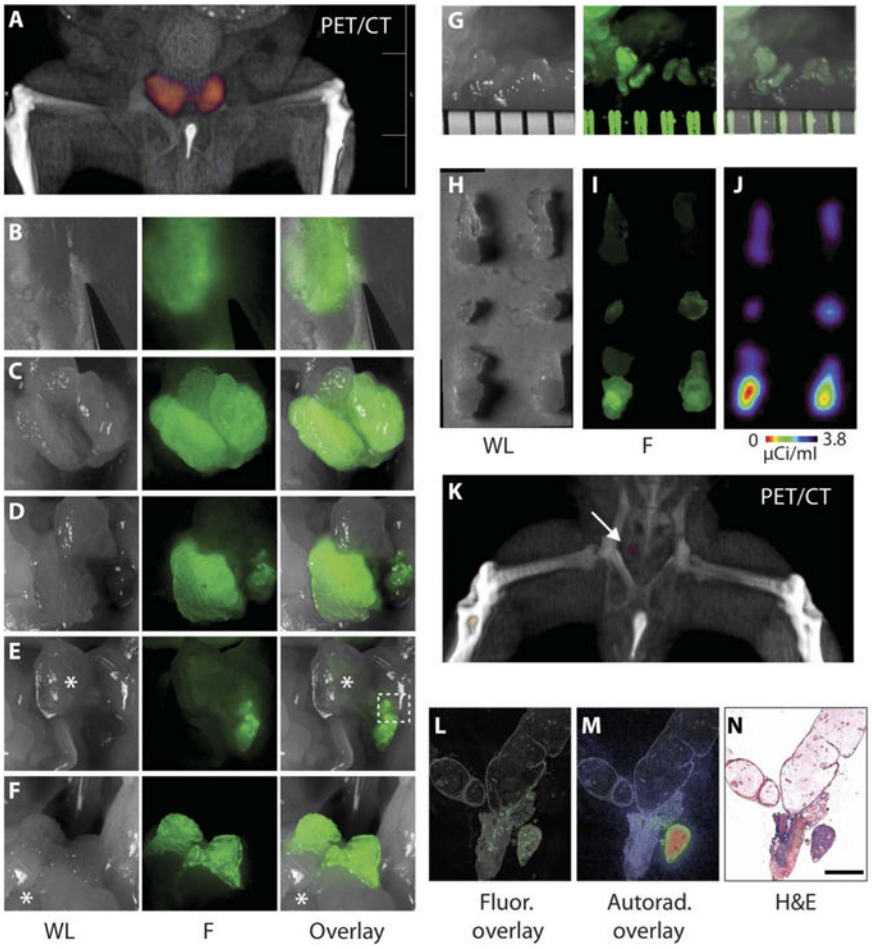

Fig. 7. Multimodality imaging for preoperative and intraoperative guidance and postoperative confirmation

(**A**) Volume-rendered PET/CT demonstrates localization of signal in the prostate for preoperative planning. **(B** to **G)** White light (WL) (left), fluorescence (F) (middle), and composite (right) images obtained at different stages during dissection of the prostate. (B) Detection of fluorescence corresponding to prostate lobes through an intact peritoneum and abdomen. (C) Fluorescence signal outlines the hK2-positive tissue of the intact ventral prostate lobes. (D) An intact right ventral prostate lobe after left lobe removal. (E) Imaging after gross removal of both ventral lobes. Bladder indicated with an asterisk. (F) Delineation of intact dorsal-lateral lobes after rostral-caudal manipulation of the bladder (*). (G) Stereoscope magnification (ruler separations are about 800 μm) of area outlined in (E). **(H** to **J)** The resected prostate lobes imaged with conventional white light (H), fluorescence (I), and radio signal (J). **(K)** Postsurgical PET/CT reveals a small remnant focus of signal (arrow). **(L** and **M)** After excision at autopsy, seminal vesicles, urethra, and remnant tissue were sectioned and imaged by fluorescence microscopy (L) and autoradiography (M). **(N)** H&E stain confirmed adenocarcinoma (scale bar, 500 μm).